Draft version April 25, 2018
Typeset using LaTeX **modern** style in AASTeX62

A Prototype Lower-VHF Radiometry System at the Long Wavelength Array

LWA Memo #208

F.K. Schinzel,[1,2] J. Craig,[1] M. Dexter,[3] J. Dowell,[1] T. Eftekhari,[1,4] J. Kocz,[5,4] S. Ellingson,[6] L. Greenhill,[4] K. Obenberger,[1,7] D. Price,[4,3] G.B. Taylor,[1] and D. Werthimer[3]

[1] *Department of Physics and Astronomy, University of New Mexico, Albuquerque, NM 87131, USA*
[2] *National Radio Astronomy Observatory, P.O. Box O, Socorro, NM 87801, USA*
[3] *Space Science Laboratory, University of California, Berkeley, CA 94720, USA*
[4] *Harvard-Smithsonian Center for Astrophysics, 60 Garden Street, Cambridge, Massachusetts, 02138, USA*
[5] *California Institute of Technology, Pasadena, CA 91109, USA*
[6] *Dept. of Electrical & Computer Engineering, Virginia Tech, Blacksburg VA 24061*
[7] *Space Vehicles Directorate, Air Force Research Laboratory, Kirtland AFB, New Mexico, USA*

ABSTRACT

The Large Aperture Experiment to Detect the Dark Ages (LEDA) has the goal to detect the sky-averaged absorption spectrum of the HI 21cm line from the intergalactic medium at $15 < z < 30$ which manifests through a broad spectral feature. In order to take first steps toward achieving this goal, a prototype system was developed at the first station of the Long Wavelength Array (LWA1) to explore the feasibility and to provide the technical advances required for this endeavor. The deployed system consists of a 64 input digital backend based on a hybrid FPGA/GPU FX correlator design. This is combined with newly designed frontend electronics that allows absolute calibration of the sky-averaged power. Here we provide an overview of the experimental setup and investigations from first observations of this system, informing technical challenges for this difficult measurement. This includes investigation of systematics in the deployed system, long-term stability of the system, and calibrated sky observations. This system, in its current state, already provides a platform for continued development of cosmological observations. In addition, it is already able to provide valuable monitoring capabilities on the conditions of the ionosphere above the array and for absolute flux calibration of astronomical observations in concert with routine LWA1 observations, especially providing the zero spacing flux for interferometric observations.

1. INTRODUCTION

The Large Aperture Experiment to Detect the Dark Ages (Greenhill & Bernardi 2012)[1] aims to measure the sky-averaged absorption spectrum of the HI 21cm line from the intergalactic medium at $15 < z < 30$, as seen against the cosmic microwave background. The goal is to characterize the thermal history of the universe through the end of the cosmological Dark Age and onset of X-ray heating of the intergalactic medium (Pritchard & Loeb 2012). Measurements with a single dipole principally allows the extraction of the absorption signature imprinted on the sky-averaged spectrum. These measurements are challenging both from the calibration and from the data analysis perspectives where the expected signal is of the order of 50 mK – 100 mK depending on the model assumptions, see e.g. (Fialkov et al. 2014), and is superimposed with the ∼3000 K foreground emission. The LEDA concept combines antennas outfitted for radiometry together with a large-N interferometric array that allows to directly derive in-situ calibrations of e.g. sky models, broadband polarized antenna gain patterns, and helps with calibrating out ionospheric fluctuations. Here we present the additions made by the LEDA project to the first station of the Long Wavelength Array (LWA1).

The LWA1 is located near the center of the NRAO managed Very Large Array in New Mexico, USA. The LWA1 array configuration is optimized to be an element for a larger beam-forming array. Even though LWA1 is conceived as just one element of many, it is currently a dedicated radio telescope distinct from, but supportive of, the separate effort to build a long-baseline aperture synthesis instrument. A detailed description of the LWA1 station architecture can be found in Taylor et al. (2012) and Ellingson et al. (2013)[2]. In 2013, driven by the LEDA project, a second array was constructed at Owen's Valley Radio Observatory (LWA-OVRO) under the lead of Caltech, which is currently undergoing early science and commissioning observations (Hallinan 2016)[3]. While LWA1 is optimized for beam-forming as part of a larger instrument and has a well-filled compact aperture, LWA-OVRO is optimized for all-sky imaging with an emphasis on longer baselines up to a few km in length.

Similar approaches to the LEDA total sky power measurements have been mostly focused on the detection of the Epoch of Reionization, which is expected to be a weak excess of emission detectable in the range of 70–200 MHz, e.g. the Experiment to Detect the Global EoR Step (EDGES; Bowman et al. 2008), the Broadband Instrument for Global HydrOgen ReioNisation Signal (BIGHORNS; Sokolowski et al. 2015), the "Sonda Cosmológica de las Islas para la Detección de Hidrógeno Neutro" (SCI-HI; Voytek et al. 2014), or the Shaped Antenna measurement of the background RAdio Spectrum (SARAS; Patra et al. 2015).

In Section 2, we provide an overview of the additions made to LWA1 to accommodate the LEDA prototype system. This includes the description of the deployed

[1] https://www.ledatelescope.org/
[2] http://lwa.phys.unm.edu/
[3] http://www.tauceti.caltech.edu/lwa/

digital backend, required modifications to the signal paths to allow non-interfering observations with LWA1, and the design and construction of "outrigger" dipoles with specialized frontend electronics for total sky-power radiometry. Section 3 contains a description of characterization and commissioning tests conducted with the deployed LEDA hardware. This is followed by a brief summary, conclusions, and outlook in Section 4.

2. HARDWARE AND SPECIFICATIONS

To accommodate the LEDA prototype system at LWA1, a range of modifications were made: alterations to the signal paths of a subset of LWA1 antennas (Sec. 2.1), the installation of additional dipoles separated from the core array (Sec. 2.2), the design and installation of a new digital backend allowing wide bandwidth full correlations of a subset of dipoles (Sec. 2.3), and the addition of a total power capture system for radiometry (Sec. 2.4).

2.1. *Signal Path*

For this project, custom built signal splitters are used to pass 64 signal paths coming from the output of the LWA1 analog receivers to both the LEDA prototype backend and the LWA1 digital backend. This allows for independent regular operations of LWA1 alongside LEDA and reduces the need for re-routing and re-wiring antenna signals manually into the LEDA digital backend. After analog filtering and amplification, the dipoles signals are output on RJ45 cables with each cable carrying two cross-dipoles. The analog signal splitters were designed into four shielded boxes, each accommodating the circuitry for 4x4 signals, differential pair analog inputs. Each balanced pair is first converted to unbalanced (single-ended) with a 2:1 transformer (Minicircuits TCM2-1T+) and split into two signals with Minicircuits TCP-2-10 splitter/combiner. Each signal then goes to a failsafe switch (Hittite HMC550E) that provides high-isolation on/off control for each possible operating combination. This allows control over the output of the signals both to LEDA and the LWA1 digital backend (DP) or respectively to LEDA/DP only. The signals for DP are output through standard RJ45 connectors, while the split signals for LEDA are aggregated onto a single Samtec Vport connector type VPSTP[4] going onto a high density shielded twisted pair cable with 16 pairs each connecting to the LEDA backend described in Section 2.3. The Vport connector was chosen due to limited space available for pass-throughs into the shielded rack, housing the LEDA prototype digital backend. This has also the advantage of fewer cables required to connect from the splitter boxes to the bulkheads. In Figure 1 one of the four assembled splitter boxes is shown together with a block diagram of the described splitter design.

The physical location of the selected 64 signal paths, which corresponds to 32 cross-dipoles, is shown in Fig. 2. This configuration was chosen to provide a uniform

[4] This connector type was discontinued by Samtec after 2012.

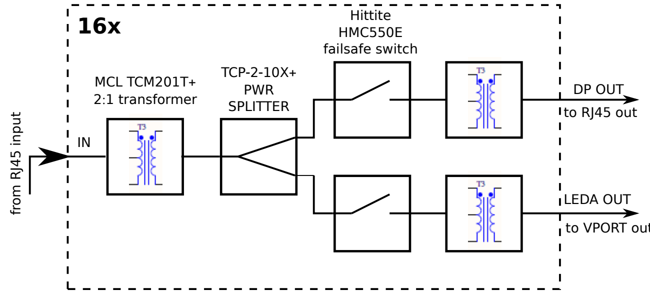

Figure 1. *Left:* One of the four splitter boxes assembled, the RJ45 pass-throughs on the sides connect the inputs, the top RJ45 pass-throughs connect the outputs. The Vport connector is seen to the lower left. The DIN 41524 connector provides access to control the output states. *Right:* Block diagram for one of the 16 channels of each splitter box.

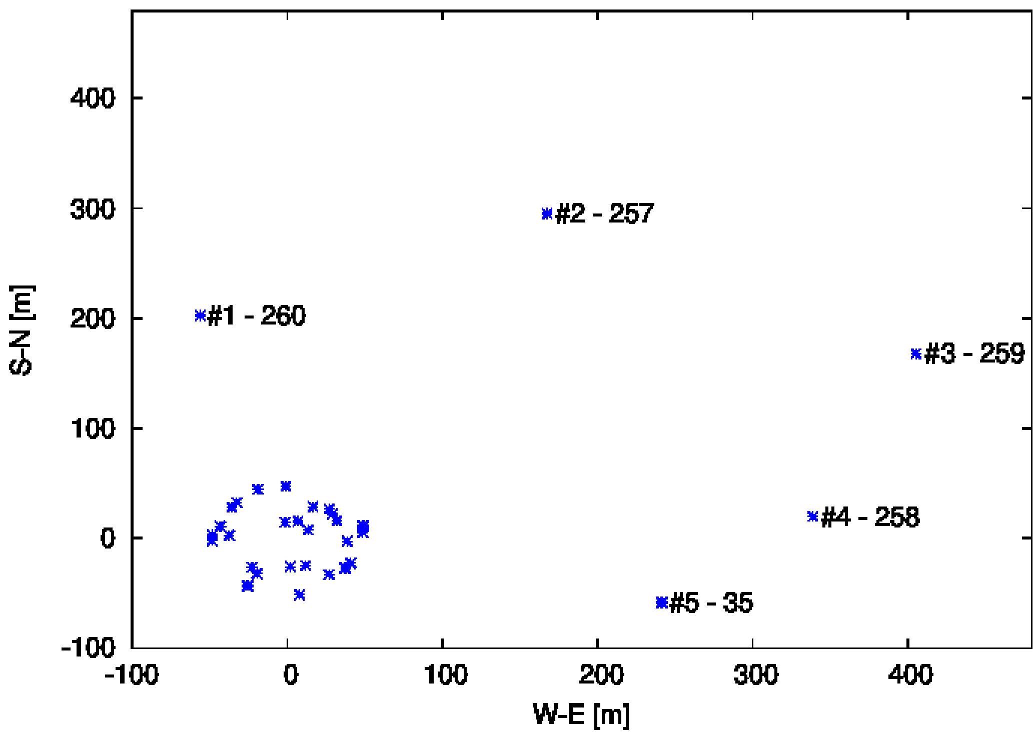

Figure 2. Configuration of the selected 64 signals from 32 cross-dipoles passed to the LEDA digital backend at LWA1. With the outrigger numbers marked for reference, see Sec. 2.2. The plot origin marks the center of the core LWA1 array.

coverage of the Fourier plane using a limited number of LWA1 dipoles and to include "outrigger" dipoles well separated from the core array. For further information on "outriggers" see Sec. 2.2. In Table 1 we list the coordinates of the selected dipoles, together with their antenna stand identification number. A more detailed listing of the technical parameters, like cable mapping, can be found in Schinzel & Dowell (2013).

2.2. *Outrigger Antennas*

Table 1. Parameters of the dipoles selected for the LEDA digital backend. Figure 2 illustrates the configuration with respect to the origin of the array.

Stand #	x^1	y^1	z^1	FEE type^2
229	+40.879	-22.745	+2.163	LWA1
154	+26.813	-33.107	+2.598	LWA1
260	+167.559	+295.101	-5.692	LEDA
198	+31.936	+16.216	+0.928	LWA1
207	+37.328	-27.243	+2.292	LWA1
215	+38.546	-2.728	+1.561	LWA1
018	-1.004	+47.373	+0.142	LWA1
252	-48.237	+2.938	+1.572	LWA1
259	+405.278	+167.840	-1.462	LEDA
121	-18.961	+44.288	+0.092	LWA1
020	+7.905	-51.405	+3.153	LWA1
257	-56.028	+202.187	-5.687	LEDA
035	+241.373	-58.617	+2.882	LEDA
108	+13.358	+7.672	+1.216	LWA1
203	-32.628	+32.437	+0.567	LWA1
258	+338.911	+19.778	+1.670	LWA1
157	-22.802	-26.433	+2.369	LWA1
174	+26.906	+26.732	+0.474	LWA1
226	-35.852	+28.440	+0.763	LWA1
240	-43.194	+10.904	+1.395	LWA1
127	-19.651	-32.303	+2.562	LWA1
153	-28.816	-37.441	+2.704	LWA1
123	-25.670	-43.331	+2.794	LWA1
172	+29.113	+22.236	+0.739	LWA1
253	+48.643	+5.271	+1.278	LWA1
006	+1.885	-26.034	+2.298	LWA1
255	+48.814	+11.217	+1.178	LWA1
064	+11.743	-24.907	+2.300	LWA1
012	-1.338	+14.429	+1.052	LWA1
042	+6.985	+15.420	+1.006	LWA1
250	-48.592	-2.249	+1.717	LWA1
114	+16.652	+28.583	+0.485	LWA1

Notes:
[1] in units of m with respect to the center of the LWA1 array, marked by a monument in the field and with the approximate coordinates of latitude 34.068891° and longitude -107.628367°. A positive x coordinate lies East of the origin, a positive y coordinate lies North of the origin, z corresponds to the elevation ~1.5m above ground.

[2] notes which type of frontend electronics is used (LWA1 production or LEDA switching).

Additional dipoles were added to the LWA1 core array to supplement its resolution and to reduce the effect of mutual coupling for those particular dipoles. In the following we refer to those dipoles as “outriggers”, which are of the same design as

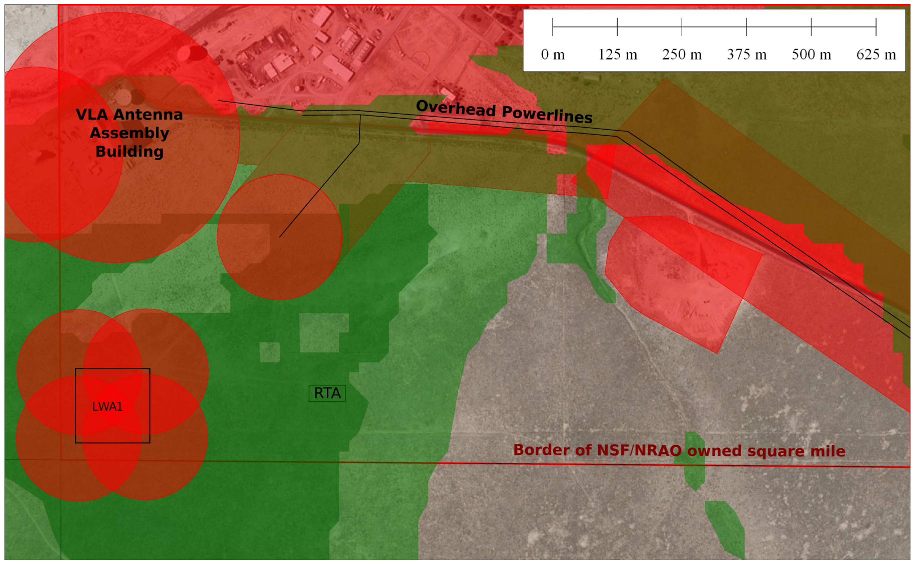

Figure 3. Aerial imagery of the area surrounding LWA1. Red areas mark regions that were excluded by the boundary conditions described in Section 2.2, shades of green from bright to dark mark the common plane with LWA1 of the terrain with the color range from dark to bright indicating the maximum allowable deviation of 1 m and 5 m respectively. The RTA marks a fenced area East of LWA1 where one dipole was placed for cable delay calibration purposes. The black solid lines indicate overhead powerlines.

LWA1 dipoles. These outriggers are to be used to provide total power time series, while the improved resolution of the array can be used to refine the formulation of the point source component of a sky model. The long baselines provided by the outriggers decrease the low-spatial-frequency component of the sky noise correlation, and increases fringe rates, which improves the performance of fringe-rate filtering. Although LEDA does not anticipate the use of fringe-rate filtering, it benefits from decorrelation of unwanted signals and thus allows for better point-source-based calibration and diagnostics (Ellingson 2011). In long wavelength arrays, mutual coupling between antenna elements results in fluctuation of beam gains and sidelobe levels when the antenna spacing is less than a few wavelengths. For outriggers suitable for the LEDA project this means the farther the outriggers are from each other the better, but no less than a few hundred meters, which in case of LEDA translates to about 10-20 wavelengths and minimizes mutual coupling. For antenna separations of 100 m the sky noise correlation becomes minimal. Between 38 and 74 MHz, the sky noise correlation combined with the effect of mutual coupling reduces the senstivity by only a few percent for pointings more than 20° away from zenith (Ellingson 2011).

The construction of outriggers was heavily constrained by additional requirements: they had to lie within the NRAO/NSF owned square mile, must be at least 200 m away from the VLA antenna assembly building, must be at least 140 m away from any VLA antenna pad, at least 100 m away from overhead power lines, at least 5 m away from any metallic fence, and must be separated from LWA1 or any other antenna element by at least 150 m. Additionally, the antennas should fall within the same

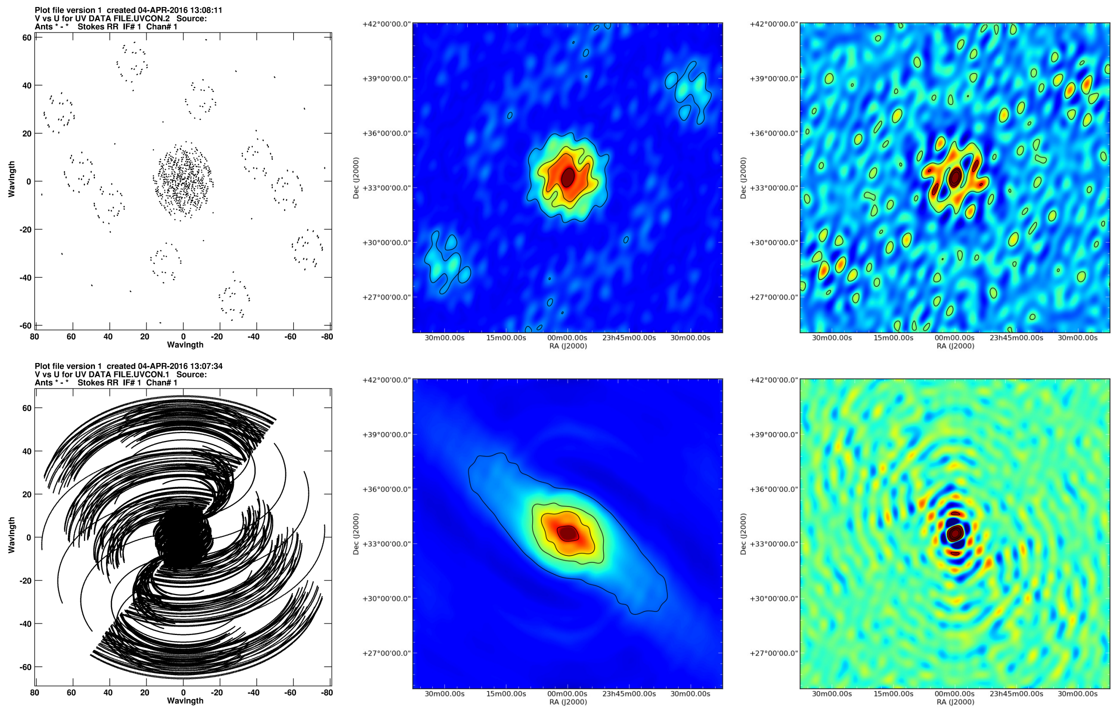

Figure 4. The top row shows the snapshot u, v-coverage of 5 outriggers combined with the LWA1 core dipoles from Table 1 at 50 MHz. The center column represents the resulting beam with natural weighting, the right column corresponds to the beam pattern with uniform weighting. The bottom row shows the resulting u, v-coverage and beam patterns for a 12 hour integration of the 32 dipoles. The contour levels for the beam plots are 70%, 50%, 35%, and 10% of the peak value, which corresponds to about -1.5, -3.0, -6.0, and -10 dB, respectively.

horizontal plane as the core-array of LWA1 with <5 m deviation. In Figure 3 we show a map with green shaded areas that represent areas matching the common plane with LWA1 with an acceptable deviation of up to 1 and 5 m (shades of green from dark to light). The entire area deviates by less than 10 m from the common plane with LWA1. We selected a Reuleaux triangle configuration for placement of dipoles (Keto 1997). The triangle was chosen to have one leg pass across LWA1 and covering a diameter of 450 m. One outrigger was placed near the North-West corner of the triangle (#1), one along the East-West extent (#2), one at the North-East corner (#3), and one at the area marked RTA (#4), a fifth outrigger was placed between the Rapid Test Array (RTA) area and LWA1 (#5), as indicated in Fig. 2. This configuration provides a maximum baseline length of about 510 m. Configurations with larger maximum baseline lengths of about 800 m were not feasible under the given constraints and if all legs of the triangle were to be populated. The resulting simulated u,v-coverages for such a sparse array are shown in Fig. 4.

Since outrigger #4 East of the core array already existed, only 4 additional outriggers had be constructed (#1,#2,#3,#5). The areas around each of those outriggers were fenced using vinyl fencing to prevent cattle from disturbing the dipoles while avoiding mutual coupling with metal structures in the vicinity of the dipoles. The fenced areas have a size of about 5x5 m each, corresponding to the dimension of the ground screen. Each of the fenced areas is connected with two LMR400 buried coaxial cables for the two polarizations of the dipoles. For future purposes a separate power cable and a 6-strand fiber optical cable connecting to the LWA1 electronics shelter were also added to allow transmitting the analog signals over fiber optics if so desired.

2.3. *Digital Backend*

The analog signals arriving from the splitter boxes are directly passed to four separate analog digital converter cards that were designed for this project. Each card has four Hittite HMCAD1511 8-bit analog digital converter (ADC) integrated circuits which allows for a maximum of 16 analog differential inputs to be digitized per ADC card. The ADC card was developed for LEDA through the Collaboration for Astronomy Signal Processing and Electronic Research (CASPER) at University of California, Berkeley[5]. Each of these cards are attached to one of the expansion ports of a standard ROACH2 revision 2 board that includes an enhanced RISC architecture CPU (Power PC) and a Xilinx Virtex-6 SX475T FPGA. This allows for digitization and conversion to the frequency domain of up to 64 analog signals. The digitized and Fourier transformed data are then passed to GPU compute nodes forming a FPGA/GPU hybrid correlator. Kocz et al. (2014) provides a detailed description of the correlator design and correlator commissioning results using the here described setup, with further discussion of a full deployment of this design for 512 inputs at LWA-OVRO in Kocz et al. (2015). In this paper we focus on the single dipole autocorrelation output of the correlator only. The LWA1 installed configuration allows three different modes of operation. The correlator can be run with 1 s and 9 s averaging. In addition, there is a spectrometer mode that provides the full time resolution of the FFT spectra from the FPGA, however due to data rate limitations, it is only able to record data from up to four dipoles at a time. In the typical mode of operation we obtain 2400 spectral channels ranging from 29.976 - 87.552 MHz with a channel width of 24 kHz split in four different spectral windows. The correlator is run with 1 s averaging on all baselines. In post-processing non-outrigger baselines are then averaged to 9 s to reduce the total data volume, while still allowing calibration using the outriggers switched frontend electronics described in the following section. A typical night time observation of 12 hours corresponds to a data volume of 1.6 TByte at 1 s time resolution or 400 GByte averaging non-outrigger baselines to 9 s.

2.4. *Total Power Capture System*

The receiver chain of any radio telescope suffers from gain variations which are mostly due to environmental effects. In the case of LWA1 the largest contribution to short and longterm gain variations are temperature variations both within the

[5] https://casper.berkeley.edu/wiki/ADC16x250-8

shelter in which the station electronics are housed primarily due to cycling of the air conditioning units (Schinzel 2013). An even larger effect have diurnal and seasonal temperature changes affecting the pre-amplifiers embedded in the frontend electronics at each antenna stand. Altogether, these effects can amount to gain variations of the order of 10%. In order to capture the total sky power from individual dipoles and to be able to compensate for receiver gain changes, special frontend electronics were installed at each dipole, replacing the standard LWA frontend electronics boards at the antenna.

The design of these frontends is based on the three state switching concept developed for the EDGES by Bowman et al. (2008). In this concept the absolute sky temperature convolved with the dipole beam pattern can be measured by switching between the sky, an ambient load, and an ambient load plus a calibrated noise source. The sky temperature convolved with the dipole beam pattern (i.e. the antenna temperature) can then be derived by calculating for a given frequency,

$$T_{\mathrm{antenna}} = T_{\mathrm{C}} \left(\frac{P_{\mathrm{A}} - P_{\mathrm{L}}}{P_{\mathrm{C}} - P_{\mathrm{L}}} \right) + T_{\mathrm{L}}, \tag{1}$$

where P_{A} is the power on the antenna, P_{L} is the power on the load, P_{C} is the power on combined load and calibration noise, T_{C} is the excess calibration noise, and T_{L} is the ambient load temperature. Assuming *a priori* knowledge of T_{C} and T_{L}, the absolute sky temperature can be be measured by calibrating out the entire chain's bandpass characteristics.

In the first deployment of these newly designed switched frontend electronic boards the three states are selected by different bias-T voltages, detected with a comparator circuit. The temperature of the noise source and calibration load are stabilized using a semiconductor heater and are defined to be $T_{\mathrm{C}} = 370\,\mathrm{K}$ and $T_{\mathrm{L}} = 298\,\mathrm{K}$. The assembly contains a 4:1 balun (Minicircuits ADT4-6T), an electromechanical relay to control the three states, a SM-4 diode and 30 dB attenuator circuit, as well as a Minicircuits Gali-74 amplification stage (+25 dB), followed by a 200 MHz low-pass filter and a Minicircuits Gali6 amplifier (+12 dB). In Fig. 5 a picture of the manually assembled PCB as described here is shown together with a block diagram.

The antenna impedance mismatch efficiency (IME) needs to be taken into account, ignoring possible ground reflections, in order to determine the sky temperature. The IME is defined as $1 - |\Gamma|^2$. Where Γ is the reflection coefficient, defined as:

$$\Gamma = \frac{Z_{\mathrm{pre}} - Z_{\mathrm{a}}}{Z_{\mathrm{pre}} + Z_{\mathrm{a}}}, \tag{2}$$

where Z_{pre} is the input impedance of the pre-amplifier (including balun) and Z_{a} is the antenna self-impedance. The expected IME of a LWA dipole into $200\,\Omega$ is shown in Fig. 6, which is based on simulations of the LWA1 dipole design described by Hicks et al. (2012) and assuming a real-valued input impedance. A direct measurement of the IME is extremely challenging at long wavelengths, future work will address

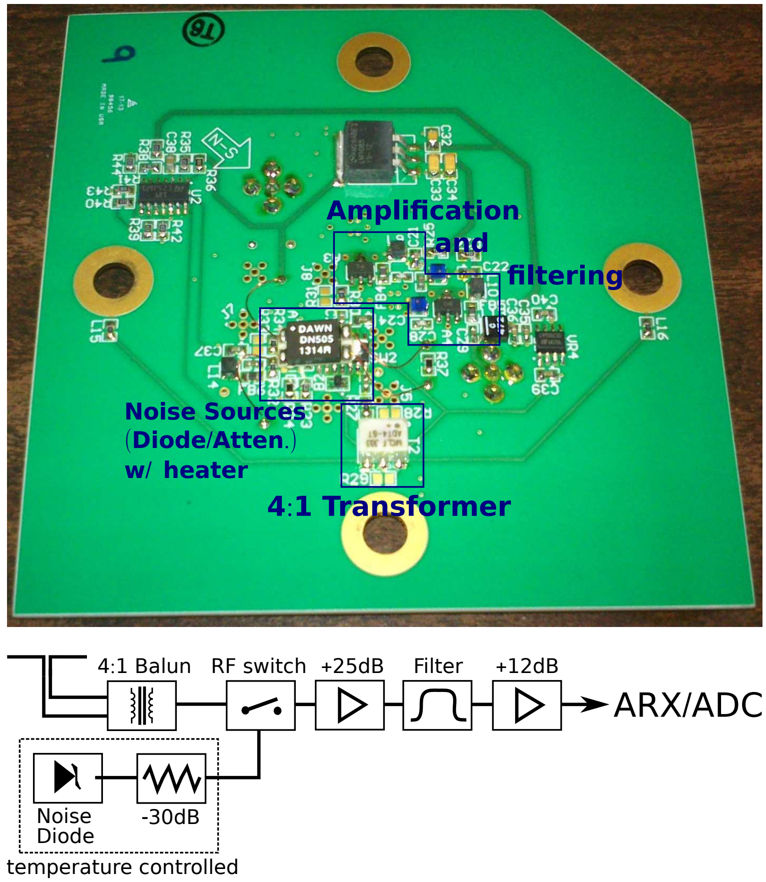

Figure 5. *Top:* A picture of one polarization of the frontend electronics of the total power capture system, featuring a three state switching scheme between sky, load, and load plus noise source. This board represents the second revision before a thermal housing was added around the temperature stabilized components. *Bottom:* Block diagram of the radio frequency components of the frontend electronics pictured on the top.

deviations of the model from the field deployed dipoles. The expected calibrated antenna temperature is then, $T_{\rm antenna} = (IME)\,T_{\rm sky}$. The impedance mismatch of the frontend was chosen to avoid or minimize spectral inflection points in order not to be confused with the expected cosmological signal, which is expected to be of the shape of a spectral trough.

Typically, the analog receiver input at LWA1 provides a Bias-T DC voltage of +15 V to power the frontend electronics using the same coaxial cable on which the radio frequency signal is broadcast. In order to provide a control over the switching states (+15 V, +16 V, and +17 V), small Bias-T boards were added to the signal chain allowing one to manually set a voltage level that can be preset using three step attenuators. These boards also allow an automatic advance through a TTL signal, for which we used the pulse per second from the station clock. Thus in this mode, the three states are cycled through in 1 s steps. For the outriggers outfitted with switching frontends a DC-block was added at the input of the LWA1 analog receiver end. The radio frequency only signal is then connected to the Bias-T board, which

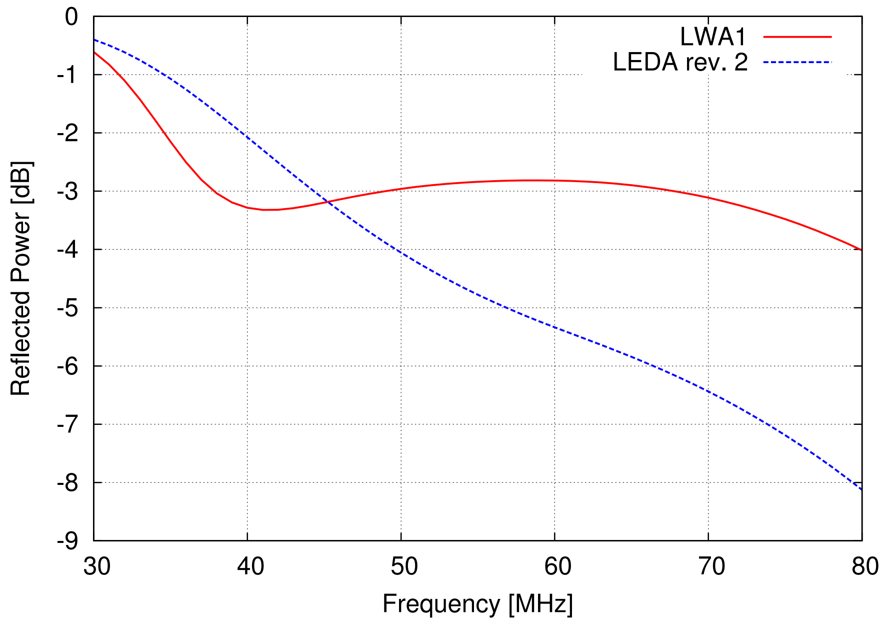

Figure 6. Simulated LWA dipole antenna impedance mismatch efficiency, shown in terms of reflected power, into a $200\,\Omega$ impedance (LEDA rev. 2), compared to the regular $100\,\Omega$ of LWA1 frontends.

adds the corresponding voltage level, which is applied to the frontend electronics. Each Bias-T board is designed to handle two signal paths, to ensure that the two polarizations on each outrigger antenna are in the same state at all times. During 2015, the Bias-T boards were revised to allow full remote control over switching cycles using a micro-controller. The typical settle times for the voltage level changes are on the order of $500\,\mu$s – 4 ms.

3. CHARACTERIZATION AND FIRST MEASUREMENTS

In this section we discuss first measurements using the above described components. The goal of these measurements was to obtain a first understanding of the radio frequency environment at LWA1, to determine system stability, and to validate the total power calibration strategy using the switching frontends.

3.1. *Commissioning Tests of Outriggers*

After construction of the outriggers was complete, the antenna stands were equipped with LWA1-type frontend electronics. The goal in this stage was to perform intial signal path testing and to commission the outrigger dipoles using the well understood LWA1 digital backend. We performed initial correlation tests that showed unexpected features in the magnitudes and phases of the correlation products. Most noticeable were strong DC offsets in the fringe rate plots for most of the baselines which in turn desensitized those baselines to the point that they were not usable as is. This lead to a detailed analysis of the issue which is summarized in the following.

Different scenarios that could explain the observed strong DC components were explored. On a system intrinsic level, signal cross-talk as well as common modes can be the cause of strong DC components. Initial investigation of strong DC components found in cross-correlation of individual dipoles from narrowband timeseries voltage captures revealed a persistent pattern of high DC components from correlations of dipoles with signal paths going through adjacent channels on a given analog receiver board. This led to the conclusion that enhanced cross-talk is present for signals using the same RJ45 output of the analog receiver board and in most cases results in a dramatically increased DC component when correlating those signals with each other. In addition, the routing of traces on the analog receiver boards are conducive to cross-talk and noise pick-up. In-situ measurements of this cross-talk using a signal generator determined an isolation of 12.2 – 46.8 dB depending on the channel pairs (Schinzel & Dowell 2014). This has significant consequences for the quality of correlation products and potentially reduces the fidelity of sky maps obtained from the inclusion of all baselines, but could also affect the quality of single dipole data. To minimize this effect for the outriggers, the signal paths of the outriggers were separated to use five different RJ45 cables on different analog receiver boards.

However, eliminating all possible instrumental causes of high DC components we further investigated using baseline combinations of all five outriggers. We performed observations with the LWA1 digital backend and found that the stand combinations 257–260, 258–259, and 108–35 showed particularly high DC offsets. The only logical explanation that could be found for those strong DC components was of external nature. Most affected by the DC offset were stand #257 (outrigger #1) and #260 (outrigger #2), in particular East-West polarization baselines. The possible source of this external interference are the powerlines running in East-West configuration providing power for LWA1 and the VLA. In a subsequent observation in November 2013 the presence and time variability of powerline RFI was confirmed with outrigger #1 being the closest to the VLA antenna assembly building. Powerline RFI was identified to be stronger while it was raining at the site, correlating with the intensity of the rain recorded by the LWA1 weather station (Schinzel & Dowell 2013). The DC components for all LEDA64 baselines were extracted for a period of low RFI that was identified from the dataset. After removal of baselines that have signals sharing the same RJ45 connection, the resulting distribution of DC components does not show significant outliers and no high levels on long baselines. Since these tests were performed, the powerline interference environment was significantly improved by working with the powerline company, Socorro Electric Coop, to overhaul the entire powerline infrastructure within the vicinity of LWA1 during the week of June 2nd – 6th, 2014. The most commonly replaced part were the worn out ties holding the conductor wire on the insulator producing air gaps for arcing, those were replaced with new factory-formed ties and splices.

3.2. *Total Power Measurements*

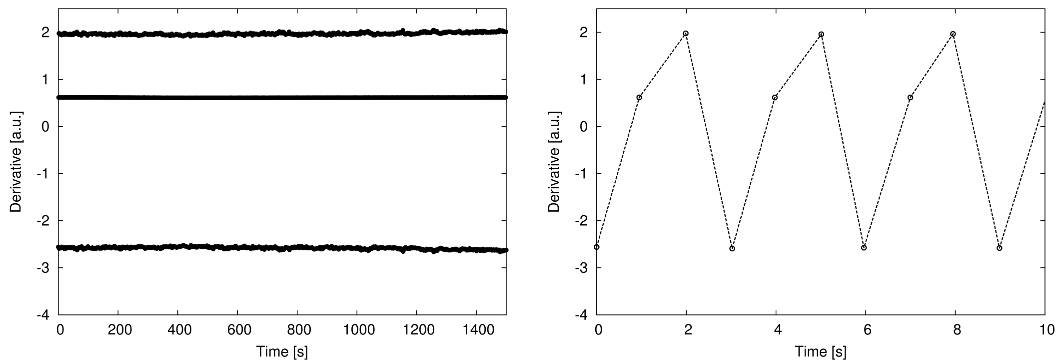

Figure 7. The left shows the obtained derivative values from the 1 s averaged spectral power to determine the three different states. The right plot is a zoom to the first 10 s of the dataset.

We conducted first commissioning observations at the end of 2013 and during the first observing season in spring 2014. We used the full time resolution spectrometer mode to verify consistent frontend state switching, to determine the rise and fall times of state changes, and to verify day-to-day system stability and repdroducability. We adopted calculating the derivative of the time series in order to automate determination of the time of state changes. After having confirmed that the high time resolution data is captured correctly, the averaging time was increased to 1 s matching the 1 s state changes. Since the station clock pulse-per-second is used both for timing of the FPGAs of the digital backend and for switching the states at the frontend, each 1 s bin corresponds to data from one of the three states. An example on how well the derivative of the state changes can be determined in 1 s data is shown in Fig. 7. This also demonstrates the stability of the system and that the derivative is a reliable way to automatically assign 1 s bins to their corresponding state. Thus we obtain a spectrum for each state every 3 s, which are shown on the left in Fig. 8. In order to attenuate low frequency RFI the analog receivers were configured to attenuate the signals below 42 MHz.

In the following, the three state calibration is performed by calculating the antenna temperature following Equation 1 for each group of 3 states and each of the 2400 spectral windows. The calibrated spectrum from 45–88 MHz is shown on the right in Fig. 8, together with a model for the expected sky spectrum based on the global sky model by de Oliveira-Costa et al. (2008). The data from 30-45 MHz corresponds to the lowest spectral window of the correlator. It was flagged due to the analog receiver filters set to attenuate the spectrum below 42 MHz to mitigate radio interference. At first glance the overall spectral shapes are in agreement with what is detected. In order to better visualize the residuals, the sky model is subtracted from the data. The residual spectrum is shown in Fig. 9. The large ripples correspond to a wavelength of 6 m and are attributed to ground reflections that have not been taken into account. Those ground reflections are fitted using an exponential decay convolved with a cosine-

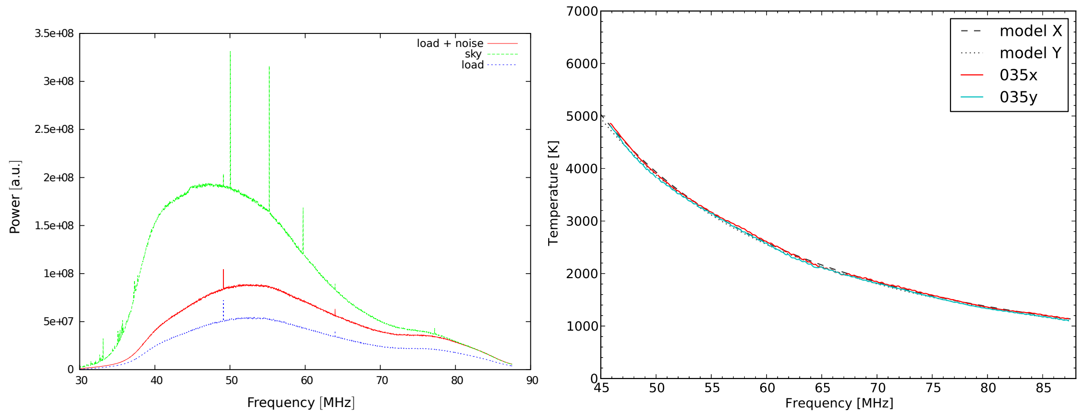

Figure 8. Left: Spectra of each of the three switching states from a single polarization, showing the sky, load (30 dB attenuator), and load+noise (30 db attenuator together with SM-4 noise diode turned on). Right: Calibrated spectrum with sky models for both polarizations.

like wave function,

$$R(x) = e^{-x \cdot a} \cdot b \cdot \cos\left(c \cdot x + d + \frac{f}{x}\right) + g, \tag{3}$$

where a, b, c, d, e and f are free parameters to be fitted. The resulting residuals after removal of the ground reflection is shown for a single polarization on the right bottom curve in Fig. 9. The residual ripples of order $\pm 20\,$K were identified to be due to standing waves and reflections along the signal path. By adding attenuation into the signal path, especially on the output side of the amplification stages of the frontend electronics, the amplitude of those ripples can be dramatically reduced, as illustrated by the top three curves in the right plot of Fig. 9, where increasing attenuation was applied from 3 dB to 9 dB reducing the ripples to residual levels of around a few Kelvin. Despite reducing the noise level, we were not able to completely eliminate these systematics. Thus precludes deep integrations required for the detection of a cosmological signal with this generation of frontend electronics. In next generation designs this issue can be addressed by adding attenuation directly between amplification stages in order to further reduce reverse gain and selecting amplifiers with lower reverse gain. In addition, the solid-state switch could be replaced by an electromechanical switch or a design could be chosen where the noise signal is mixed with the sky signal, avoiding the need for switching states completely. Also, having the noise signals of comparable power to the sky signal would potentially reduce effects causing variations in the reverse gain that are not removed through three state switching.

Following verification of system operability, we conducted nightly observations between February 20th and May 29th, 2014 to verify system stability over a longer time period. Radio frequency interference was excised using the sum-thresholding technique which is described in Offringa et al. (2013). With this flagging method we typically removed less than 11% of the entire data. In Figures 10 and 11 we show the resulting time series and waterfall plots of the relative difference in calibrated

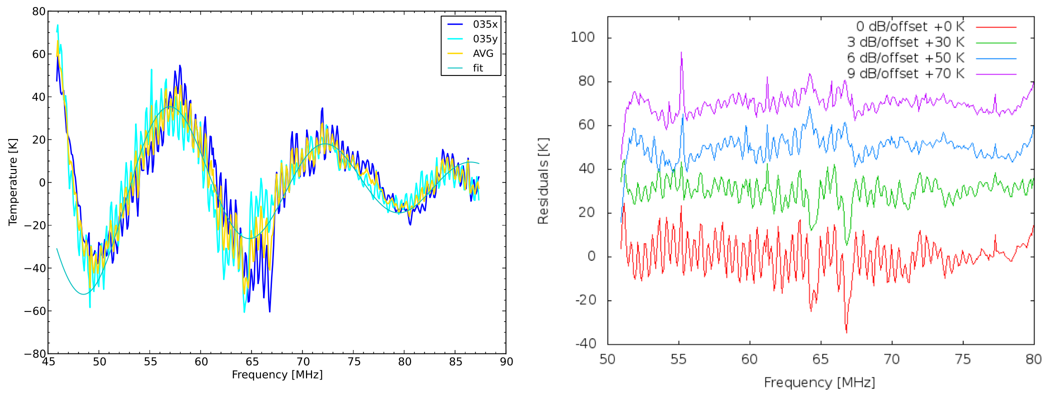

Figure 9. Left: Residuals for outrigger #5 obtained on March 14, 2014 for a 1 hour period covering 10.5 – 11.5 local sidereal time. The fit curve to the average residuals was determined applying Eqn. 3. Right: Residuals after ground reflection is removed for different attenuation levels of the signal path between frontend electronics and analog receivers.

sky power for 16 non-consecutive days for two hours centered around 11.0h LST between March 8th and March 29th, 2014. Especially around 70 MHz weak RFI that remained in the data after flagging can be seen at the 3-5% level. Figure 10 shows that the relative differences from day to day increase from $\pm 1.0\,\%$ up to $\pm 3.5\,\%$ toward lower frequencies. Also, X polarization is more affected than Y polarization. This is explained by the intrinsic properties of the ionosphere, where attenuation and emission effects become more pronounced toward lower frequencies. Also during days of high broadband values around days 4–10, the remaining RFI is also pronounced and is most likely due to radio transmitters reflecting off the ionospheric E-layer that typically forms in spring and summer at LWA1 latitudes. The more pronounced effects in X polarization are most likely due to a higher sensitivity to structures in the Galactic emission. However, the day-to-day variations, as well as the increase in variation toward lower frequencies, can also be explained by the presence of strong powerline RFI. We anticipate to repeat similar measurements in the future to better characterize the ionospheric conditions following the mitigation of strong powerline RFI. Despite this, these first observations indicate the day-to-day variation for a quiet ionosphere can be expected to be less than 1% in absolute power and most likely will not pose a significant problem for cosmological observations.

Finally, we present a 12 hour calibrated sky drift curve from outrigger #5 observed on March 14, 2014, shown in Fig. 12. In this figure both a single frequency curve at 74 MHz and the waterfall plots between 45 and 88 MHz for each polarization are plotted. From the waterfall plot one can see that RFI flagging was performed, however the amount of required flagging is very small, demonstrating the excellent RFI quiet environment at the LWA1 site. These observations were performed before a major overhaul of the nearby powerlines and thus are affected by power line RFI primarily in X polarization, which can be seen as horizontal features in the waterfall plot. The observations were performed during night time when the majority of the

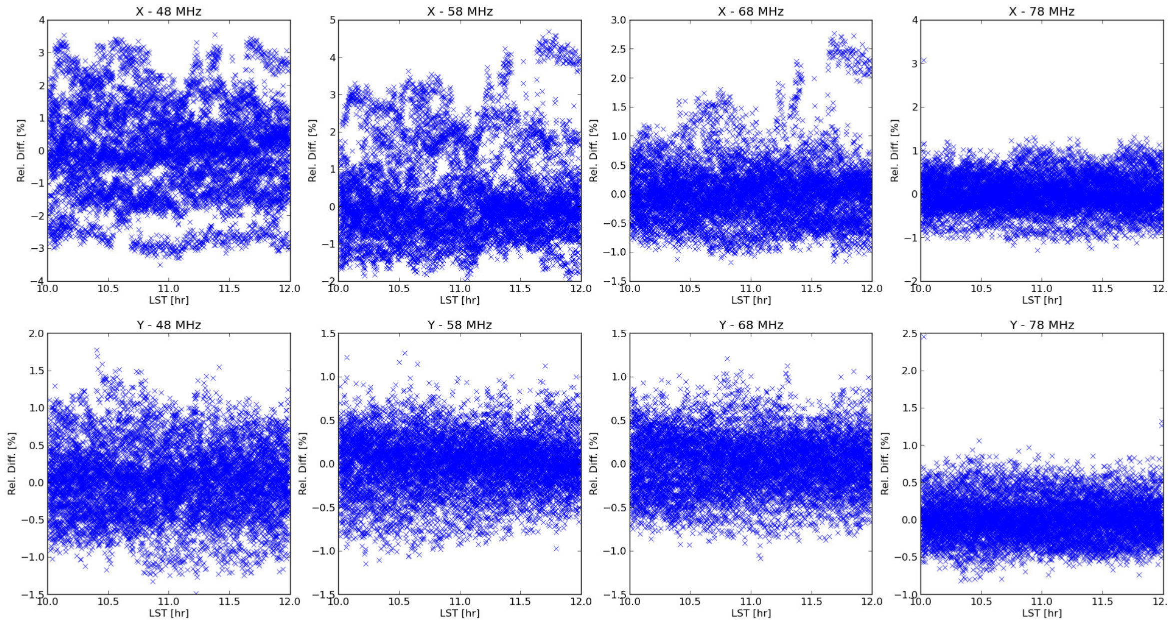

Figure 10. Time series plots of the relative difference for 48, 58, 68, and 78 MHz averaged over 1 MHz of bandwidth each covering a time period of 16 days between 2014/03/08 to 2014/03/29 of data recorded from stand #35 covering LSTs from 10 - 12h. The two polarizations are shown separately.

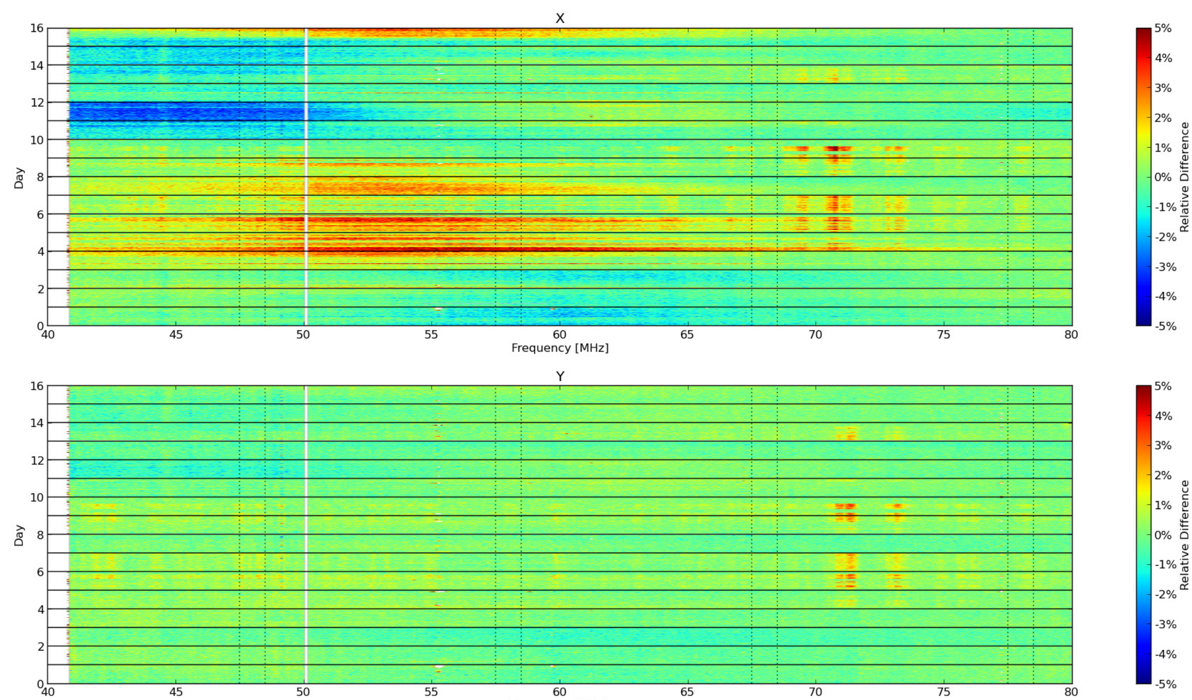

Figure 11. Waterfall plots of the relative difference for several frequencies averaged over 1 MHz of bandwidth covering a time period of 16 days between 2014/03/08 to 2014/03/29 of data recorded from stand #35 covering LSTs from 10 - 12h. The two polarizations are shown separately.

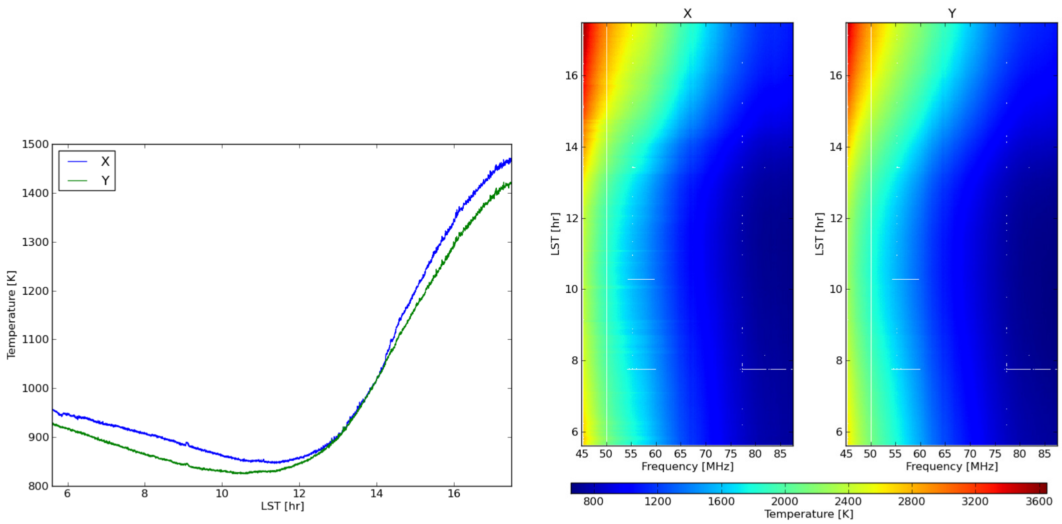

Figure 12. *Left:* Total power calibrated sky drift curve for 74 MHz for each polarization. *Right:* Total power calibrated sky drift spectrum for 45 – 88 MHz for each polarization.

Galactic plane was not high on the sky. Toward the end one can see the galaxy rising through the increase in observed total sky power starting around 12 h local sidereal time (LST).

4. SUMMARY & CONCLUSIONS

Here we described the successful deployment of a prototype system to allow absolute total power measurements with single dipoles in combination with the adjacent LWA1 array. We described the placement of additional dipoles around the LWA1 core array, the modifications that were made to the LWA1 signal paths, including the addition of a separate digital backend. Development and deployment of special switching frontends was of particular focus. These allow calibration of the recorded total power signal using the EDGES three state switching scheme, providing in-situ corrections for gain changes in the receive system.

The system was tested for systematic limitations and long-term stability that could affect future cosmological observations. In the process of this we noticed increased cross-talk between channels in the analog receivers. As a consequence of which we have already partially addressed this in a new analog receiver design that was deployed at a new LWA1-like station at Sevilleta National Wildlife Refuge. It uses an updated design of the analog receiver boards where the input signal traces were better isolated, mitigating cross-talk and noise pick-up. In addition, we note that an alternative connector for the analog signal output with better signal isolation could be used in future upgrades, which is a modification of the RJ45 connector currently used, namely ARJ45.

We performed residual measurements of the newly designed frontend electronics to check for systematic limitations in the calibrated total power data and check for its suitability for detecting the cosmic dawn signal. Those first measurements revealed ground reflection ripples at the level of ± 40 K over a sky signal of 2000-6000 K. By fitting and removing those large ripples we were able to obtain residuals of ± 10 K. This corresponds to a removal of foregrounds by a factor of 100–300. We demonstrated that added attenuation reduces reflections within the signal path and thus the residuals could be reduced to a few Kelvin. This is clearly not enough to achieve a detection of a cosmological signal that is of the order of mK. However, future iterative improvements to the frontend electronic designs are informed by these preliminary measurementes where we anticipate to address current limiting systematics to push residuals into the mK regime. We anticipate to improve the frontend electronics in future iterations: providing better isolation of the amplification stages, bringing the noise levels of the reference noise sources closer to that of the sky temperature. This has the goal to achieve residual levels that are close to the expected thermal noise limits, which will then allow integration of the observed sky power. Some of these issues we have already addressed in a new design of the switching frontends which will be discussed in Price et al. (2016) and Bernardi et al. (2016).

We performed observations on a day-to-day basis over the course of a month in order to test the overall system stability. It turned out to be remarkably stable with the strongest influence on the observed average power being the ionosphere and powerline RFI at levels of $\sim$4%, which makes the existing system suitable for radiometric monitoring of ionospheric conditions. In addition, observations of the total power with this instrumentation is used for zero-spacing absolute flux calibration of astronomical all-sky maps produced using all 256 dipoles of the LWA1 array (Dowell et al. 2016) providing an improved model of the foreground emission of the sky, which will be required to achieve detection of the predicted cosmological signal.

The deployed system will facilitate and enable measurements with future frontend electronics aiming to detect the cosmological signal that is expected to be found in the total sky power. In addition, similar measurements are also able to be performed with the well tested LWA1 digital backend for better comparison of instrument systematics. Ultimately it will be possible to verify and confirm similar measurements undertaken in a different radio frequency interference environment than at LWA-OVRO in combination with simultanous sky and antenna calibration provided by the full cross-correlated array in California.

ACKNOWLEDGEMENTS

LEDA research is supported by NSF grants AST/1106059, AST-1105949, and PHY/0835713. LEDA and related research has received generous support in the form of hardware donations from Nvidia, Hewlett Packard, and Xilinx. Construction of the LWA1 has been supported by the Office of Naval Research under Contract N00014-07-C-0147. Support for operations and continuing development of the LWA1 is provided by the National Science Foundation under grants AST-1139963 and AST-

1139974 of the University Radio Observatory program. Particular thank goes to the support by staff from the National Radio Astronomy Observatory.

REFERENCES

Bernardi, G., Zwart, J., Price, D., et al. 2016, in prep.

Bowman, J. D., Rogers, A. E. E., & Hewitt, J. N. 2008, ApJ, 676, 1

de Oliveira-Costa, A., Tegmark, M., Gaensler, B. M., et al. 2008, MNRAS, 388, 247

Dowell, J., Taylor, G. B., Schinzel, F. K., & Kassim, N. E. 2016, submitted to MNRAS

Ellingson, S. 2011, Antennas and Propagation, IEEE Transactions on, 59, Issue 6, 1855

Ellingson, S. W., Taylor, G. B., Craig, J., et al. 2013, IEEE Transactions on Antennas and Propagation, 61, 2540

Fialkov, A., Barkana, R., & Visbal, E. 2014, Nature, 506, 197

Greenhill, L. J., & Bernardi, G. 2012, ArXiv e-prints, arXiv:1201.1700

Hallinan, G. a. a. 2016, in prep.

Hicks, B. C., Paravastu-Dalal, N., Stewart, K. P., et al. 2012, PASP, 124, 1090

Keto, E. 1997, ApJ, 475, 843

Kocz, J., Greenhill, L. J., Barsdell, B. R., et al. 2014, Journal of Astronomical Instrumentation, 3, 1450002

—. 2015, Journal of Astronomical Instrumentation, 4, 1550003

Offringa, A. R., de Bruyn, A. G., Zaroubi, S., et al. 2013, Astronomy & Astrophysics, 549, A11

Patra, N., Subrahmanyan, R., Sethi, S., Udaya Shankar, N., & Raghunathan, A. 2015, ApJ, 801, 138

Price, D., Greenhill, L., Ellingson, S., et al. 2016, in prep.

Pritchard, J. R., & Loeb, A. 2012, Reports on Progress in Physics, 75, 086901

Schinzel, F. 2013, LWA Memo Series, #198

Schinzel, F. K., & Dowell, J. D. 2013, DC component analysis at LWA1, Tech. rep., LWA Memo #200

—. 2014, In-situ testing of frequency labeling and aliasing of DP and measurement of signal cross-coupling at LWA1, Tech. rep., LWA Memo #201

Sokolowski, M., Tremblay, S. E., Wayth, R. B., et al. 2015, PASA, 32, e004

Taylor, G. B., Ellingson, S. W., Kassim, N. E., et al. 2012, Journal of Astronomical Instrumentation, 1, 50004

Voytek, T. C., Natarajan, A., Jáuregui García, J. M., Peterson, J. B., & López-Cruz, O. 2014, ApJL, 782, L9